Adaptive Finite Element Methods in Geodynamics; Convection Dominated Mid–Ocean Ridge and Subduction Zone Simulations

D. R. Davies [1,2], J. H. Davies [1*], O. Hassan [2], K. Morgan [2] and P. Nithiarasu [2]

[1] School of Earth, Ocean & Planetary Sciences, Cardiff University, Wales, UK.

[2] School of Civil & Computational Engineering, Swansea University, Wales, UK.

Abstract

Purpose: An adaptive finite element procedure is presented for improving the quality of convection dominated mid–ocean ridge and subduction zone problems in geodynamics.

Approach: The method adapts the mesh automatically around regions of high solution gradient, yielding enhanced resolution of the associated flow features. The approach utilizes an automatic, unstructured mesh generator and a finite element flow solver. Mesh adaptation is accomplished through mesh regeneration, employing information provided by an interpolation based local error estimator, obtained from the computed solution on an existing mesh.

Findings: The proposed methodology works remarkably well at improving solution accuracy for both mid–ocean ridge and subduction zone simulations. Furthermore, the method is computationally highly efficient.

Originality of paper: To date, successful goal–orientated/error–guided grid adaptation techniques have, to our knowledge, not been utilized within the field of geodynamics. This paper presents the first true geodynamical application of such methods.

Keywords: Finite element method, unstructured mesh, adaptivity, error indicator, geodynamics, mid–ocean ridge, subduction zone.

1 Introduction

Over recent decades, adaptive grid techniques (see Babuska & Rheinbolt, 1978; Lohner *et al.* 1985 and Peraire *et al.* 1987) have been widely employed by the engineering community, in areas ranging from compressible aerodynamics (e.g. Hassan *et al.* 1995) to incompressible flow and heat transfer problems (Pelletier & Ilinca 1995; Nithiarasu & Zienkiewicz 2000; Mayne *et al.* 2000). However, until recently (Davies *et al.* 2007), grid adaptivity had

*Correspondence to J. Huw Davies, School of Earth, Ocean & Planetary Sciences, Cardiff University, Main Building, Park Place, Cardiff, UK, CF10 3YE. e-mail: DaviesJH2@cf.ac.uk

not been applied within the field of geodynamics, a branch of geophysics concerned with measuring, modeling, and interpreting the configuration and motion of Earth's crust and mantle. This is surprising, since the method provides a suitable means to solve many of the complex problems currently encountered in the field. The motivation behind this study, therefore, is to further emphasize the point that such techniques are extremely useful within a geophysical framework.

The mantle, the region between Earth's crust and core, contains 84% of Earth's volume and 68% of its mass, but because it is separated from direct observation by the thin crust there are many unsolved problems. Mantle convection establishes one of the longest time scales of our planet. Earth's mantle, though solid, is deforming slowly by a process of viscous creep and, while sluggish in human terms, the rate of this subsolidus convection is remarkable by any standard. Indeed, estimates of the mantle's Rayleigh number, quantifying its convective instability, range between 10^6 and 10^8, generating flow velocities of 1–10 cm yr^{-1}. Plate tectonics is the prime surface expression of this convection (Davies & Richards 1992), although ultimately all large scale geological activity and dynamics of the planet, such as mountain building and continental drift, involve the release of potential energy within the mantle. Consequently, innovative techniques for simulating these large scale, infinite Prandtl number convective systems are of great importance.

Rather than simulate the whole mantle, which would require massively parallel codes in 3D spherical geometry, this investigation focusses upon geologically active regions along Earth's surface, where the mantle interacts with Earth's crust. Steady state thermal convection is examined, at a Mid–Ocean Ridge (MOR) and at a Subduction Zone (SZ), problems that can be well approximated in two dimensions. A MOR is a long, elevated volcanic structure, occurring at divergent plate margins along the middle of the ocean floor. Such ridges form through the symmetrical spreading of two tectonic plates from the ridge axis. SZ, on the other hand, occur at convergent plate margins, where Earth's tectonic plates move towards each other, with one plate subducting beneath the other into Earth's mantle. The geometry of a SZ is mapped out by the locations of earthquakes and deep seismicity, with most present day SZs extending from trenches on the ocean floor, at an angle ranging from near horizontal to near vertical, to a depth of up to 700 km. Volcanoes tend to form $\approx$ 100km above the subducting slab, at the volcanic arc, making SZs the most active tectonic locations on our planet.

Numerical simulations of these tectonic settings tend to be characterized by the interaction of complex geometries, complex material properties and complex boundary conditions. Such a combination often yields unpredictable and intricate solutions, where narrow regions of high solution gradient are found embedded in a more passive background flow. These high gradient regions present a serious challenge for computational methods: their location and extent is difficult to determine *a priori*, since they are not necessarily restricted to the boundary layers of the domain. Furthermore, even if their location is identified, with the current methods employed in the field, it is often impossible to resolve localized features. It is

natural to think, therefore, that grid adaptivity, with *a posteriori* error indication criterion, could play an important role in the development of efficient solution techniques for such problems.

The present study extends on the work of Davies *et al.* (2007), which applied grid adaptivity to infinite Prandtl number, thermal and thermo–chemical convection. However, here, attention is focussed on geodynamical application, as opposed to methodology formulation and validation. The aim is to improve the solution quality of MOR and SZ simulations, by utilizing adaptive refinement strategies. Results, which are consistent with those previously published in the literature, illustrate that the method is advantageous, improving solution accuracy whilst reducing computational cost.

The remainder of this paper will cover the equations governing mantle convection, together with the numerical and adaptive strategies used in their solution. An overview of the error indicator and remeshing technique is then provided and, to conclude, the methodology is applied in geodynamical simulations of the tectonic settings introduced above.

2 Methodology

2.1 Governing Equations and Solution Procedure

Earth's mantle is solid. However, over large timescales it deforms slowly through processes such as dislocation and diffusion creep. As a consequence, motion within Earth's mantle can be described by the equations governing fluid dynamics. Since the mantle has an extremely large viscosity ($\approx 10^{21}$ Pa), the equations governing mantle convection are somewhat different to those governing the more typical fluid mechanics problems:

1. The large viscosity of Earth's mantle makes the Prandtl Number (Pr), the ratio between viscous and inertial forces, of the order 10^{24}. Accordingly, inertial terms in the momentum equation can be ignored.

2. The Ekman number (i.e. the ratio between viscous and Coriolis forces) is of the order 10^{9}, since the velocity of convection within the mantle is so small. As a consequence, the Coriolis force can be neglected.

3. The centrifugal force, which causes the ratio of the major to the minor radius of Earth to depart from unity by only one part in three hundred, is proportional to the square of the velocity. Consequently, it is even smaller than the Coriolis force and it is also ignored.

This mantle convection problem is formulated in terms of the conservation equations of momentum, mass and energy, expressed in the dimensionless, vector form

$$\nabla^2 \mathbf{u} = -\nabla p + Ra\, T\, \mathbf{k} \tag{1}$$

$$\nabla \cdot \mathbf{u} = 0 \tag{2}$$

$$\frac{\partial T}{\partial t} = \mathbf{u} \cdot \nabla T + \nabla^2 T \tag{3}$$

where $\mathbf{u}$ is the velocity vector, T is the temperature, p is the non–lithostatic pressure, $\mathbf{k}$ is the unit vector in the direction of gravity and t is the time. In addition, the dimensionless parameter

$$Ra = \frac{g\beta\Delta T d^3}{\kappa\nu} \tag{4}$$

denotes the Rayleigh number, where g is the acceleration due to gravity, β is the coefficient of thermal expansion, ΔT is the temperature drop across the domain, d is the domain depth, κ is the thermal diffusivity and ν is the kinematic viscosity.

A widely used 2D geodynamics finite element program, ConMan, which employs quadrilateral elements and bilinear shape functions for velocity, is utilized to solve these incompressible, infinite Prandtl number equations. The main characteristics of the code are presented here although a more detailed description can be found in King *et al.* (1990). The continuity equation is treated as a constraint on the momentum equation, and incompressibility is enforced in the solution of the momentum equation using a penalty formulation. The well known streamline upwind Petrov Galerkin (SUPG) method is used to solve the energy equation (Hughes & Brooks 1979) and an explicit second order predictor corrector algorithm is employed for time marching. Since the temperatures provide the buoyancy to drive the momentum equation and, as there is no time dependence in the momentum equation, the algorithm to solve the system is simple: given an initial temperature field, calculate the resulting velocity field. Use the velocities to advect the temperatures for the next time step and solve for a new temperature field.

2.2 Adaptive Strategies

Over recent decades, unstructured grid systems have been developed and applied in simulations of various computational fluid mechanics problems. The accuracy of a computational solution is strongly influenced by the discretization of the space in which a solution is sought. In general, the introduction of a highly dense distribution of nodes throughout the computational domain will yield a more accurate answer than a coarse distribution. However,

limitations in computer processing speed and accessible memory prohibit such a scenario. An appropriate alternative would be to improve the accuracy of the computation where needed. Grid adaptation provides a suitable means to do this, ensuring that grids are optimized for the problem under study. Broadly speaking, such adaptive procedures fall into two categories:

1. h–refinement, in which the same class of elements continue to be used, but are changed in size to provide the maximum economy in reaching the desired solution.

2. p–refinement, in which the same element size is utilized, but the order of the polynomial is increased or decreased as required.

A variant of the h–refinement method, termed adaptive remeshing, is employed in this study. It provides the greatest control of mesh size and grading to better resolve the flow features. The main advantages offered by such methods are (Lohner 1995):

1. the possibility of stretching elements when adapting features that are of lower dimensionality than the problem at hand, which leads to considerable savings;

2. the ability to accommodate, in a straightforward manner, problems with moving bodies or free surfaces.

In this method, the problem is solved initially on a coarse grid. However, this grid must be sufficiently fine to roughly capture the physics of the flow. Remeshing then involves the following steps:

1. The solution on the present grid is analyzed through an error indication procedure, to determine locations where the mesh fails to provide an adequate definition of the problem. An interpolation based local error indicator is employed in this study, based upon nodal temperature curvatures (e.g. Peraire *et al.* 1987).

2. Given the error indication information, determine the nodal spacing, δ, the value of the stretching parameter, s, and the direction of stretching, α, for the new grid.

3. Using the old grid as a background grid, remesh the computational domain utilizing a variant of the advancing front technique (George, 1971; Lo, 1985; Davies *et al.* 2007), which is capable of generating meshes that conform to a user prescribed spatial distribution of element size (i.e. δ, α and s).

4. Interpolate the original solution between meshes.

5. Continue the solution procedure on the new mesh.

The remeshing process is repeated until a desired level of accuracy has been achieved.

2.2.1 The Error Indicator

Having obtained an initial approximation to a solution for a given problem, one can improve the accuracy of this solution by adaptively refining the mesh. In this study, mesh adaptation is achieved by using the computed solution to determine 'optimum' nodal values for δ, s, and α. The mesh is then regenerated, using a variant of the advancing front technique, with the initial computational mesh acting as a background grid.

To determine the values for the mesh parameters, it is necessary to use the initial solution to give some indication of the error magnitude and direction. A certain 'key' variable must be identified and then the error indication process can be performed in terms of this variable. In this study, the error indicator is based on the temperature variable, T. Of course, other variables (e.g. pressure) or any combination of variables (e.g. temperature and velocity) can be chosen, depending upon the nature of the problem under investigation.

A local error indicator, based upon interpolation theory, is employed here. Error indicators of this nature make the assumptions that:

1. The nodal error is zero.
2. The solution is smooth.

This allows one to *approximate* the elemental error by a derivative one order higher than the element shape function. We make use of this approach to refine the grid, by considering the second derivatives (curvatures) of T. Note that for the remainder of this section we will restrict our discussion to the solution variable ϕ, rather than refer to T explicitly.

Consider a one-dimensional situation in which the exact values of the key variable ϕ are approximated by a piecewise linear function $\hat{\phi}$. The error E is then defined as:

$$E = \phi(x) - \hat{\phi}(x) \tag{5}$$

If the exact solution is a linear function of x, this error will vanish, as the approximation has been obtained using piecewise linear finite element shape functions. To a first order of approximation, the error, E, can be evaluated as the difference between a quadratic finite element solution, $\hat{\phi}$, and the linear computed solution. To obtain a piecewise quadratic approximation, one could obviously solve a new problem using quadratic shape functions. This, however, would be costly and an alternative approach for estimating a quadratic approximation from the linear finite element solution can be employed. Assuming that the nodal values of the quadratic and the linear approximations coincide i.e. that the nodal values of E are zero, a quadratic solution can be constructed on each element, once the value of the second derivative is known, assuming of course that second derivatives are constant over each element.

The variation of the error, E, within an element, e, is then expressed as:

$$E_e = \frac{1}{2}\zeta(h_e - \zeta)\frac{\partial^2\hat{\phi}}{\partial x^2} \tag{6}$$

where ζ denotes a local element coordinate and h_e denotes the element length (Peraire *et al.* 1987). The root mean square value E_e^{RMS} of this error over the element is computed as:

$$E_e^{RMS} = \left\{\int_0^{h_e} \frac{E_e^2}{h_e} d\zeta\right\}^{1/2} = \frac{1}{\sqrt{120}} h_e^2 \left|\frac{\partial^2\hat{\phi}}{\partial x^2}\right|_e \tag{7}$$

where $||$ denotes absolute value. Several previous studies (Demkowicz *et al.* 1984; Peraire *et al.* 1987; Nithiarasu, 2000) have demonstrated that equi-distribution of the element error leads to an optimal mesh and in what follows we employ the same criterion. This requirement implies that:

$$h^2\left|\frac{\partial^2\hat{\phi}}{\partial x^2}\right| = C \tag{8}$$

where C denotes a positive constant. Finally, the requirement of Equation 8 suggests that the optimal spacing δ on the new adapted mesh should be computed according to:

$$\delta^2\left|\frac{\partial^2\hat{\phi}}{\partial x^2}\right| = C \tag{9}$$

Equation 9 can be directly extended to the two-dimensional case by writing the quadratic form:

$$\delta_\beta^2(m_{ij}\beta_i\beta_j) = C \tag{10}$$

where β is an arbitrary unit vector, δ_β is the spacing along the direction of β, and m_{ij} are the components of a 2×2 symmetric matrix, $\mathbf{m}$, of second derivatives defined by:

$$m_{ij} = \frac{\partial^2\hat{\phi}}{\partial x_i \partial x_j} \tag{11}$$

These derivatives are computed at each node of the current mesh by using the two-dimensional equivalent of the variational recovery procedure (NEED REFERENCE HERE). This procedure allows one to recover the nodal values of second derivatives from the elemental values of the first derivatives of $\hat{\phi}$.

2.2.2 Adaptive Remeshing

The basic concept behind the adaptive remeshing technique is to use the computed solution to provide information on the spatial distribution of the mesh parameters. This information will be used by the mesh generator to generate a new adapted mesh in those areas where the values of the optimal mesh parameters differ from the values of the current mesh parameters by greater than a user prescribed amount, *err_max* (set as 0.5% in this study).

Optimal values for mesh parameters are calculated at each node of the current mesh. The directions $\alpha_i; i = 1, 2$ are taken to be the principal directions of the matrix $\mathbf{m}$. The corresponding mesh spacings are computed from the eigenvalues λ_i of $\mathbf{m}$, as:

$$\delta_i = \sqrt{\frac{C}{\lambda_i}}; \quad i = 1, 2 \tag{12}$$

The spatial distribution of the mesh parameters is defined when a value is specified for the constant C. The total number of elements in the adapted mesh will depend upon the choice of this constant. The magnitude of the stretching parameter, s, at node n, is simply defined as the ratio between the two spacings:

$$s_n = \sqrt{\frac{|\delta_{1n}|}{|\delta_{2n}|}} \tag{13}$$

where δ_{1n} and δ_{2n} are the spacings in principal direction 1 and 2 respectively.

In the practical implementation of this method, two threshold values are used: a minimum spacing, δ_{min}, and a maximum spacing, δ_{max}, with:

$$\delta_{min} \leq \delta_i \leq \delta_{max} \quad ; i = 1, 2 \tag{14}$$

It is apparent that in regions of uniform flow, the computed values of δ_n will be very large. Consequently, the user must specify a maximum allowable value, δ_{max}, for the local spacing on the new mesh. Then, if δ_n is such that $\delta_n \geq \delta_{max}$, the value of δ_n is set to δ_{max}. Similarly, the user prescribes a maximum allowable stretching ratio on the new mesh.

The new mesh is generated according to the computed distribution of mesh parameters. The original solution is then transferred onto the new mesh using linear interpolation and the solution procedure continues on the new mesh. It should be noted that the increase in definition of flow features is achieved by decreasing the value of δ_{min}. The value of δ_{min} is therefore the major parameter governing the number of elements in the new mesh.

It is important to note that the methodology employed in this study has previously been validated by Davies *et al.* (2007).

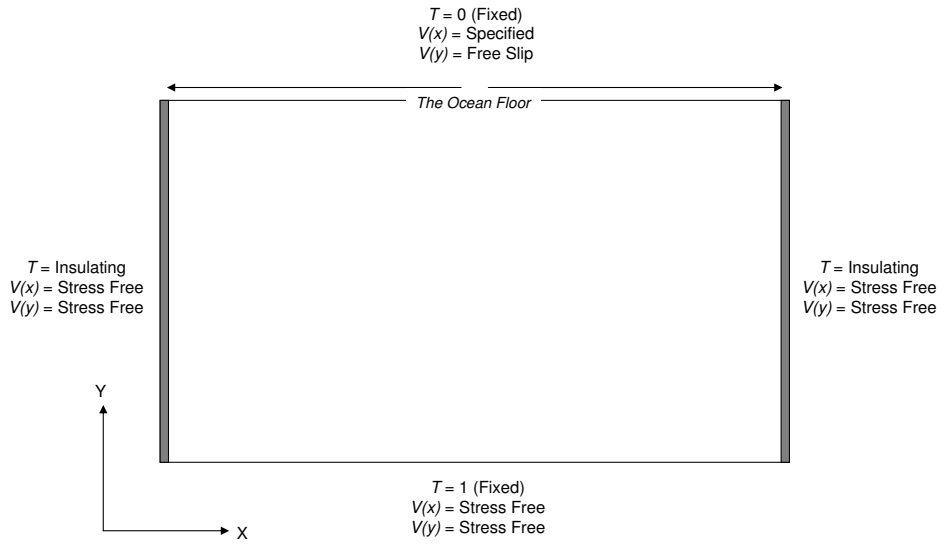

Figure 1: A summary of the boundary conditions utilized in our mid–ocean ridge model. Stress free conditions, i.e. no normal or shear stress, are employed at the lower and side boundaries, with prescribed velocities (kinematic) on the upper boundary, the non–dimensional equivalent of 5cm yr^{-1}. Temperatures are fixed on upper ($T = 0$) and lower ($T = 1$) boundaries with insulating sidewalls.

3 Geodynamical Applications

3.1 Mid–Ocean Ridge Magmatism

A significant body of work has been published on the numerical modeling of Mid–Ocean Ridges (MOR). For example, Buck *et al.* (2005) use numerical models to study modes of faulting at ridges, Kuhn & Dahm (2004) employ numerical models to study magma (i.e. molten rock) ascent beneath ridges, while Albers & Christensen (2001) study the channeling of plumes below ridges. While these models were designed to investigate specific processes at ridges, incorporating complex material properties and boundary conditions, we present a simple, generic, passive (buoyancy forces are neglected) MOR model, utilizing our results to demonstrate the benefits of grid adaptivity.

3.1.1 Model Geometry and Boundary Conditions

The model presented does not incorporate the entire convecting mantle. Instead, we focus on the region directly adjacent to a MOR. Our results are derived from simulations in a rectangular domain of height 1, which in our application to a MOR represents 500km, and width 5 (= 2500km), x being non–dimensionalized as

$$x' = \frac{x}{l_0} \tag{15}$$

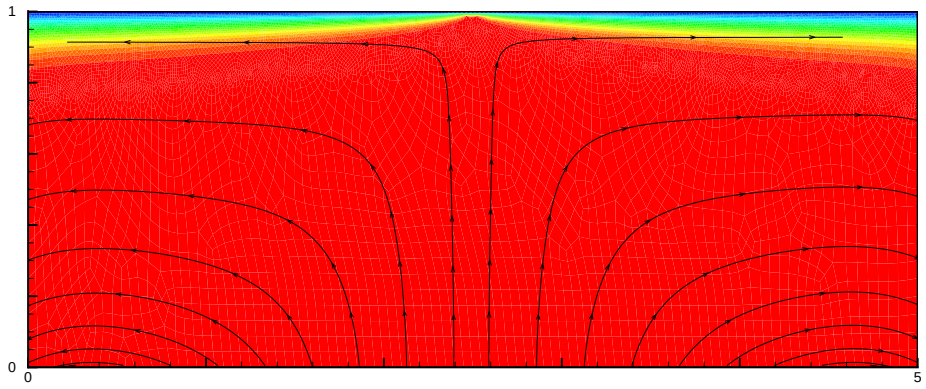

Figure 2: The thermal field generated by our mid–ocean ridge simulations. Red is hot ($T = 1$), blue is cold ($T = 0$) and the color scale is linear. A series of streamtraces are included, indicating the flow field behavior.

where $l_0 = 500$km. By limiting the vertical and horizontal extent of the domain, computational expenditure is reduced, allowing one to accurately resolve the flow details contiguous to plate boundaries. The main drawback of this technique is that flow must be permitted through the lower and side boundaries of the model; these boundary conditions are therefore specified in such a way as to mimic the effect of the full convecting system on the smaller region under study (Figure 1).

The plate motion is prescribed as a kinematic boundary condition at the upper surface. A non–dimensional velocity equivalent to 5cm yr^{-1} is chosen (similar to the values observed at fast spreading ridges), utilizing the non–dimensional relation

$$v' = \frac{v l_0}{\kappa} \tag{16}$$

where κ represents thermal diffusivity, taken as 1×10^{-6} m^{2}s^{-1}. Time is non–dimensionalized by the conductive time scale

$$t' = \frac{t l_0^2}{\kappa} \tag{17}$$

The model makes no attempt to account for forces that move the plate. The new plate that is continuously created within the model is disposed of by a prescribed rate of flow through the outer boundary. This in turn is replaced by material from the side and lower boundaries. Material properties are uniform throughout the domain, there are no internal heat sources and the Rayleigh number is set to zero.

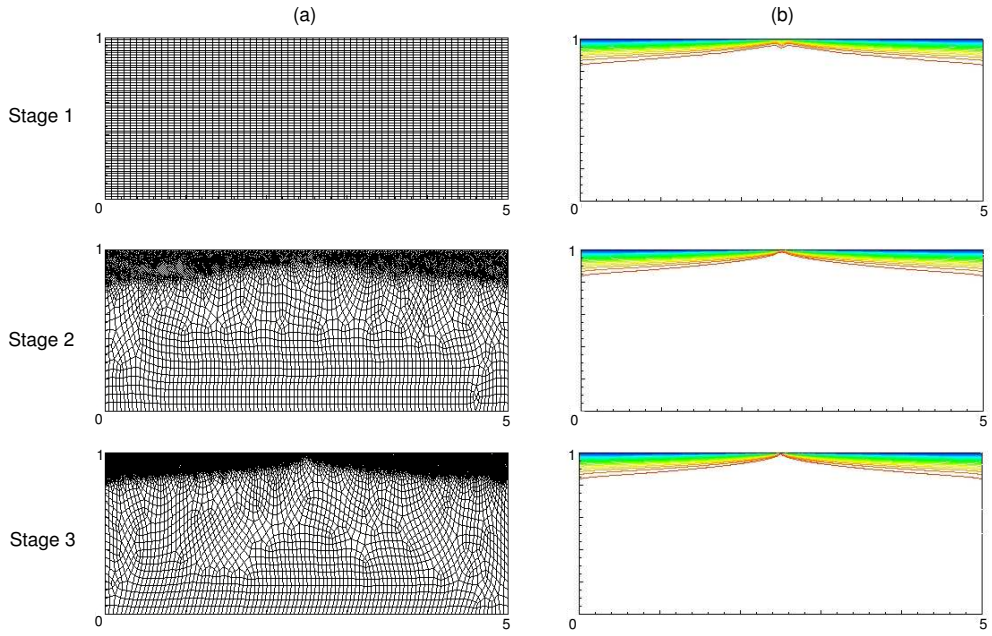

Figure 3: Evolution of the temperature field (b) on a series of adapted grids (a). Red is hot ($T = 1$), blue is cold ($T = 0$), and the contour spacing is 0.05. Note that the coordinate scales are distorted, with $x : y = 0.5$.

3.1.2 Results

We find that the broad patterns observed in previous studies are reproduced (Figure 2). With flow driven kinematically by surface 'plate' motion, the system evolves to approach a steady state. This typically involves the development of a cold 'plate' thickening with age at the surface, with flow beneath focusing heat directly towards the ridge axis (i.e. the upper center of our model). This 'plate' is particularly well captured in our simulations, as a direct consequence of the adaptive methodologies utilized. It is necessary, therefore, to provide a brief run through the evolution of the calculation. Having obtained an initial solution on a coarse grid (Figure 3–Stage 1b), mesh adaptation was invoked to resolve, in more detail, the temperature profile encountered. The solution was analyzed via the error indication procedure and the domain remeshed, utilizing the information yielded by this error indicator (the generation parameters δ_{Min}, δ_{Max}, s_{Max} and C displayed in Table 1) to control the regeneration process. The ensuing grid is displayed in Figure 3 (Stage 2a). Note that nodes have automatically clustered around zones of high temperature gradient, at the surface and immediately below 'plate' boundaries.

The solution procedure continued on this new mesh producing the thermal field observed in Figure 3 (Stage 2b). It is clear, even visually, that the solution on this grid is far better resolved than that seen in Figure 3–Stage 1b, with contours more steady and consistent. However, by examining the thermal field close to the ridge axis (Figure 4–Stage 2b) it

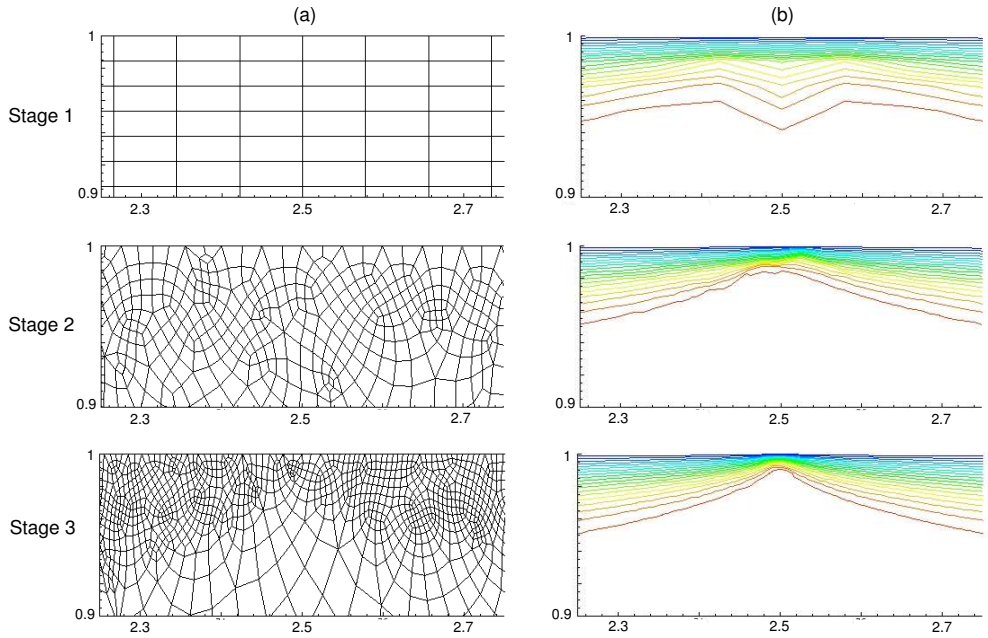

Figure 4: As in Figure 3, but at higher magnification, close to the ridge axis. Once again, red is hot ($T = 1$), blue is cold ($T = 0$), and the contour spacing is 0.05

becomes apparent that the problem remains inadequately defined. Consequently, one further remeshing loop was invoked, producing the mesh observed in Figure 3 (Stage 3a). The simulation was terminated once the solution was deemed to have converged on this mesh. The final temperature profile is displayed in Figures 3 and 4 (Stage 3b).

With each remeshing, the benefits of the multi–resolution solution permitted by the adaptive methodologies can be appreciated. Within the upper thermal boundary layer, where temperature contours are extremely compact and gradients are high, a large number of nodes is required to generate an accurate solution. Since the lower reaches of the model are more passive, with lower solution gradients, the number of nodes required for accuracy is significantly less. The proposed method automatically ensures that an 'optimal' mesh is generated, with zones of fine resolution being analogous to zones of high solution gradient. Consequently, the thermal field is accurately resolved in a computationally efficient manner.

As a quantitative test of the method, we have computed heat flow as a function of ocean floor age, at each stage of the calculation (i.e. for converged solutions on each grid). The results are displayed in Figure 5, alongside data derived from a cooling half–space model (e.g. Turcotte & Schubert, 2002) which is an analytical approximation to the problem, and data obtained from a simulation utilizing a fully uniform, structured mesh of almost $30,000$ elements (SM in Figure 5). An exceptional agreement is observed between all data sets beyond $\approx$ 1Ma (Ma = million years). This accord, however, disappears within $\approx$ 1Ma of the ridge axis. Here, the half space model tends towards infinity, whereas our simulations converge towards a finite

Stage	Elements	Nodes	δ_{min}	δ_{max}	s_{max}	C
1	4096	4225	-	-	5	-
2	12965	13259	0.01	0.1	5	0.05
3	22790	23263	0.005	0.1	5	0.03

Table 1: The sequence of meshes and mesh generation parameters employed for the mid-ocean ridge simulations. It should be noted that the initial mesh (Stage 1) was generated via a simple uniform mesh generator, as opposed to the advancing front generator typically employed throughout this study.

value, as indeed would be expected from the physics of the numerical problem. Nevertheless, this graph provides a simple way to illustrate the benefits of the proposed methodology. Simulation results show sequentially improving agreements with the half–space model as one refines the grid from Stage 1 to Stage 3. Results track the model closer to the ridge axis, culminating in successively higher values at the axis itself. This is a direct consequence of the improved resolution inherent to the adaptive methodologies utilized. At the ridge axis itself, the true numerical solution is extremely difficult to reproduce. However, what is clear from this graph is that the adaptive methodologies employed significantly improve solution quality. The results from a fully uniform structured mesh, albeit with more elements, are not competitive with those obtained using the adapted grids.

A further caveat to the adaptive refinement strategies is the fact that they are computationally highly efficiency . The uniform mesh simulation expended almost 15% more CPU time than the adaptive simulation, with figures for the adaptive case including the time allocated for remeshing. The generation of a new optimal mesh is an inexpensive procedure, typically taking between 15 and 20 time-steps, compared to the time taken for one time step with a non-changing mesh (although the time expended in remeshing can be decreased significantly by specifying a larger *err_max* - the remeshing tolerance - see Section 2.2.2). These results are consistent with those of Davies *et al.* (2007), illustrating that solutions to the MOR problem presented are not only accurate, but are also obtained in a resourceful manner.

3.2 Subduction Zone Magmatism

As is the case with mid–ocean ridges, numerical models have become central in shaping our understanding of SZ dynamics and thermal structures. Andrews & Sleep (1974) use numerical models to demonstrate that frictional heating along the subducting plate is not likely to produce enough heat to melt the slab. Davies & Stevenson (1992) cite numerical models as primary evidence to suggest that the oceanic crust of the down going slab is not melted extensively, if at all, and hence is not the source of SZ magmatism, with the possible exception of the special case of very young oceanic crust, which is hotter. Numerical simulations have also been developed for studies of SZ mineralogy and metamorphism (Peacock, 1996), transportation of water and its influence on melting (Iwamori, 1998), the thermal and dynamic evolution of the upper mantle in SZ (Kincaid & Sacks, 1997), and the effects of

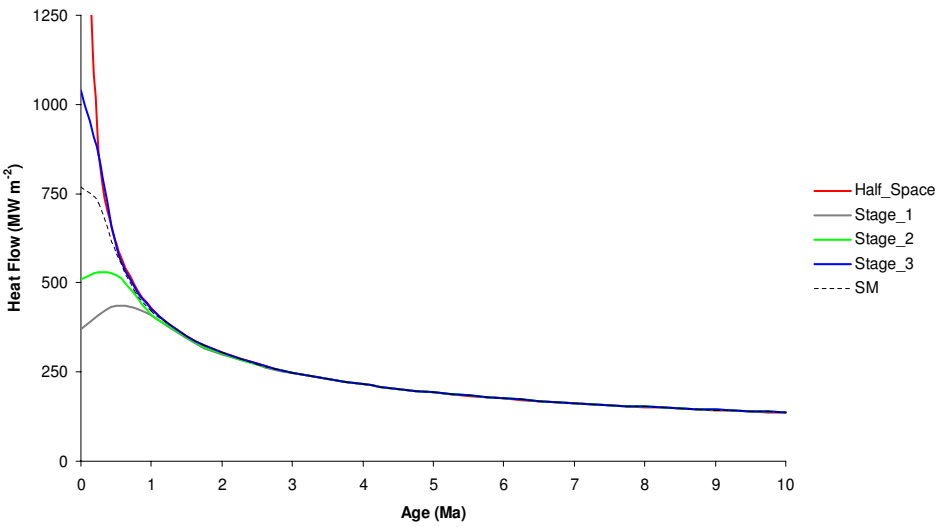

Figure 5: Plot of computed heat flow against age relation for our MOR models and the cooling half–space model for $k = 3.3$ $\mathrm{Wm^{-1}K^{-1}}$. A clear divergence is observed between the computed solution and the cooling half–space. However, as the grid becomes more and more refined, through the adaptive procedures, this divergence decreases dramatically. Note that SM represents the solution obtained on a fully uniform structured mesh. It is included for comparative purposes only.

chemical phase changes on the downwelling slab (Christensen, 2001). It is important to note that the SZ discussed here have an idealized geometry. The terminology used in describing such SZ is presented in Figure 6.

In this study, a basic isoviscous flow model is presented which is used to demonstrate the benefits of grid adaptivity within a SZ context. It is common knowledge that the most difficult region to resolve in any SZ model is the area between the subducting slab and the overriding plate, commonly known as the mantle wedge corner, as a direct consequence of a singularity at the intersection between slab and plate. Since the most geologically important processes in SZ occur here, models of wedge flow need to be carefully constructed. Previous studies have achieved higher resolution in this area by *a priori* generating a mesh with a large number of nodes clustered in the wedge, e.g. Davies & Stevenson 1992. However, this is not ideal. Grid adaptivity provides a suitable alternative, allowing one to automatically generate an optimal mesh, through *a posteriori* error indication procedures, ensuring that nodes are positioned where required. Such techniques could therefore play an important role in future solution strategies for these models, for both the steady state situations considered here and more complex unsteady problems.

3.2.1 Model Geometry and Boundary Conditions

We do not simulate the entire convecting mantle. Instead, we focus on the region directly adjacent to a generic SZ. The results of calculations using a box of 3×2 non–dimensional

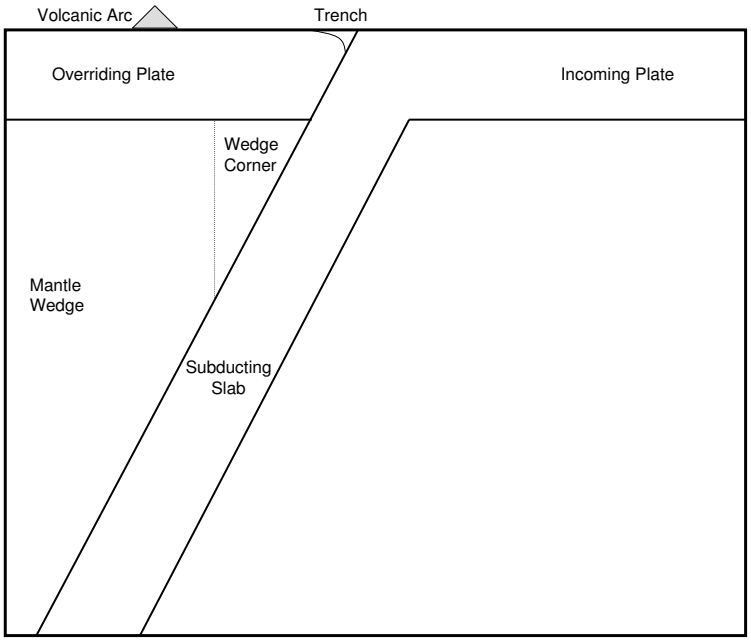

Figure 6: The geometry of a generic subduction zone. Note that by overriding plate we mean the rigid lithosphere. By wedge corner we mean the apex at which the overriding plate and slab meet. Adapted from Davies & Stevenson (1992).

units are presented, equivalent to 600×400km. Boundary conditions are summarized in Figure 7. We shall distinguish two lithospheres. First, a mechanical lithosphere, which will be considered to be the rigid part of the plate on the time scale of the process, and second, a thermal lithosphere, which is Earth's upper thermal boundary layer. The descending slab is prescribed by a kinematic boundary condition as a non–migrating slab dipping uniformly at 60^o. The subduction velocity is set to the non–dimensional equivalent of 9cm yr^{-1}. These velocities are also prescribed to the incoming plate. A zero velocity condition is specified at certain nodes to model the mechanical lithosphere of the overriding plate, corresponding to a thickness of 50km. This restricts them from participating in the viscous flow region. The thickness of the mechanical lithosphere of the downgoing plate is taken to be the same as the overriding plate (i.e. 50 km). The side and lower domain boundaries are prescribed with velocities derived from the analytical solution to a Newtonian corner flow problem (McKenzie, 1969). Indeed, by setting the model up in this way, a direct comparison can be made between simulated velocities and those of the analytical solution. This allows a quantitative demonstration into the benefits of grid adaptivity to SZ simulations. Temperature boundary conditions are slightly more complex. The temperature is fixed at the surface ($T = 0$) and a zero heat flux condition is specified at the base of the model. On the continental side, i.e. the overriding plate, the thermal boundary layer is assumed to be 100km thick. Within this layer, it is assumed that vertical heat transfer is practically by conduction alone and that

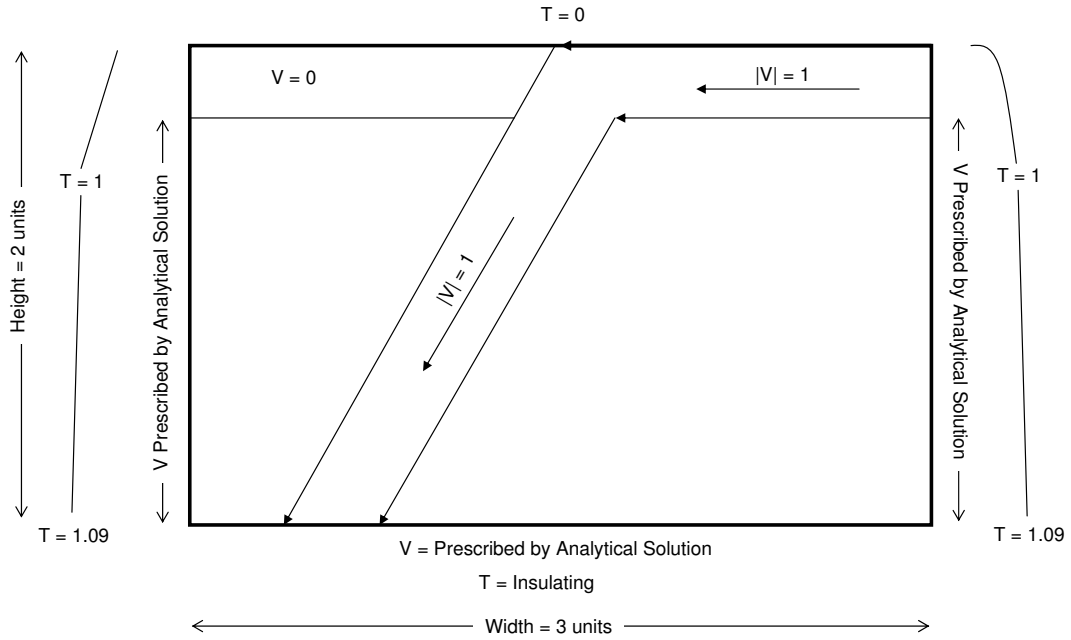

Figure 7: A composite diagram illustrating the boundary conditions utilized in the subduction zone model.

steady state conditions prevail. The temperature profile is, therefore, represented by a linear temperature gradient, with the temperature at the base of this layer assumed to be 1350^oC, or $T = 1$ in non–dimensional units, and the temperature at the top, i.e. the surface of the overriding plate, assumed to be 0^oC, or $T = 0$ in non–dimensional units. The situation on the oceanic side, i.e. the incoming plate, is slightly different. The oceanic plate is created at the axis of a mid–ocean ridge and cools as it moves away from the ridge axis, as was illustrated in Figure 2. The temperature profile within the incoming plate can, therefore, be approximated, by a standard error function, consistent with a plate of age 40Ma (Carlsaw & Jaeger 1959), as

$$T(y) = T_{(s)} + \Big\{T_{(m)} - T_{(s)}\Big\}\mathrm{erf}\Big\{\frac{y}{2\sqrt{\kappa t_{40}}}\Big\} \tag{18}$$

where t_{40} is the age of the plate in seconds, $T_{(s)}$ is the surface temperature, $T_{(m)}$ is the mantle temperature and κ is the thermal diffusivity, which is assumed to be $10^{-6}\mathrm{m}^2\mathrm{s}^{-1}$. The thermal boundary layer is assumed to be 100 km thick with temperatures at its top and base taken as $T = 0$ and $T = 1$, in non–dimensionalized units, respectively.

Convection is believed to be the dominant mode of heat transfer in the upper mantle, beneath the thermal boundary layers. Consequently, the temperature gradient is lower. In the interior of a vigorously convecting fluid, the mean temperature gradient is approximately

Stage	Elements	Nodes	δ_{min}	δ_{max}	s_{max}	C
1	7333	7499	0.06	0.06	1	-
2	17876	18131	0.02	0.04	3	0.2
3	20906	21157	0.01	0.04	3	0.1

Table 2: The sequence of meshes and mesh generation parameters employed for the subduction zone simulations

adiabatic. Considering the adiabatic temperature gradient of the uppermost mantle (Turcotte & Schubert, 1982) and the depth of the box, i.e. 400km, a temperature of 1470^{o}C is specified at the bottom left and right corners of the box, which, in non–dimensionalized units, is ≈ 1.09. The temperature increases linearly from the base of the thermal boundary layer to this point. It is important to note that there are no explicit heat sources or sinks within the model.

3.2.2 Results

Results are displayed in Figure 8. They are broadly consistent with previous SZ models, with the thermal field being characterized by rapid temperature variations over the solution domain, predominantly along the margins of the subducting plate and in Earth's upper thermal boundary layer. However, these results are not central to our study. It can be seen from Figure 8 that the adaptive procedure has refined the grid at locations of high temperature gradient, without overloading the remainder of the domain (note that a preset element size is specified for nodes in the upper mechanical lithosphere and the down going slab, since velocities here are prescribed). Such grid refinement has a dramatic effect on solution accuracy. This is illustrated in Figures 9 and 10, which display the discrepancy between simulated velocities and those yielded by the analytical solution. This local error, E_L, is calculated as

$$E_L = \frac{|V_M - V_A|}{|V_A|} \tag{19}$$

where V_M denotes simulated velocities, V_A the velocities yielded by the analytical solution and $|\cdot|$ absolute value. The improvements yielded by grid adaptivity are clear to see. On the initial mesh (Stage 1), the error is extremely prominent, emanating from its source at the mantle wedge corner and strongly degenerating the solution over a large section of the wedge. A minor error is also visible at the intersection of the incoming plate and the down going slab, although it is small in comparison to that observed in the wedge corner. By Stage 2, the re-meshing process has refined the grid considerably in these regions and, consequently, a substantial decrease in error is observed. An additional reduction in error also occurs in Stage 3, as the grid becomes further refined at these locations. Even though the effects of the

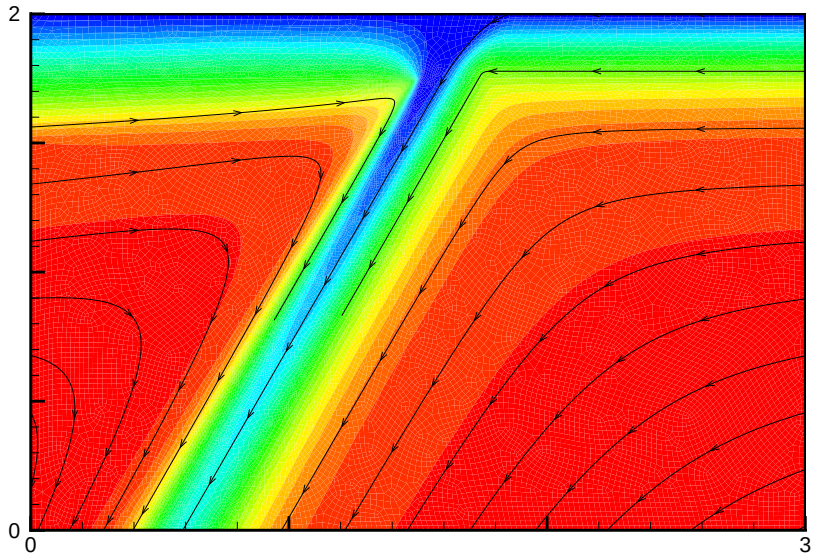

(a)

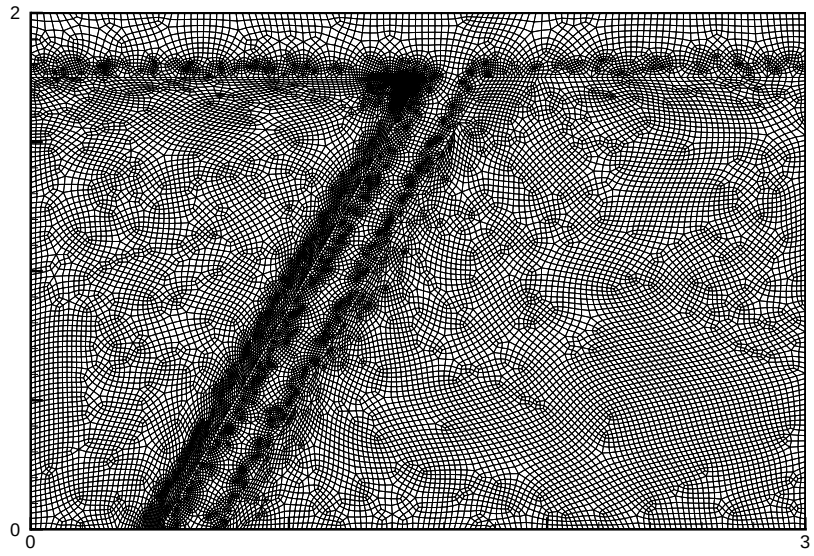

(b)

Figure 8: (a) The steady state thermal field yielded by our subduction zone simulations. Red is hot ($T = 1.09$), blue is cold ($T = 0$) and the color scale is linear. Note that the slab remains cool throughout, while the mantle wedge corner heats up significantly. The dark lines traversing the solution domain are velocity streamtraces, included to provide an indication of the direction of motion. (b) The final mesh.

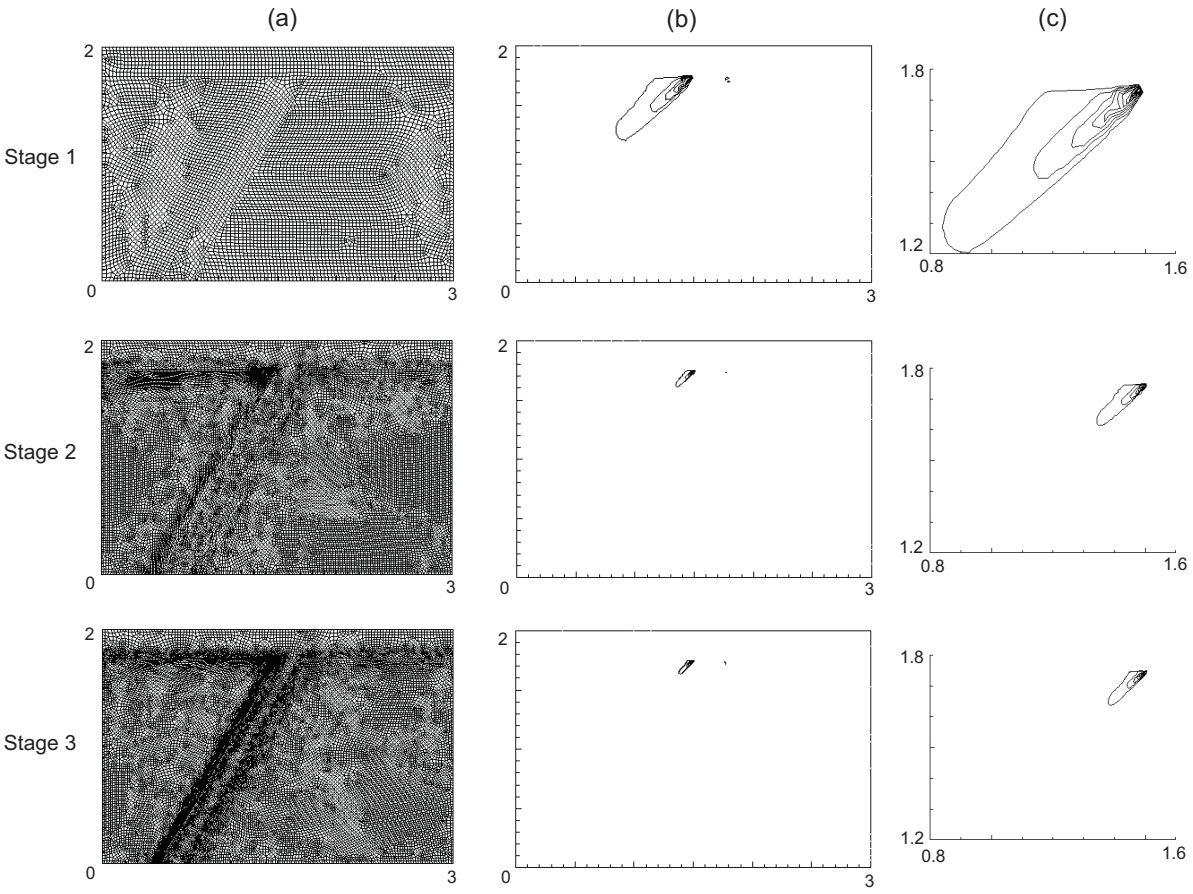

Figure 9: (a) The series of adapted grids. (b) The discrepancy between simulated and analytical velocities, E_L. (c) A high resolution image of this error in the mantle wedge corner. Contour values are not important in this figure; they are included in Figure 10. This figure merely illustrates the extent of the error decreases with each remeshing. The influence of the singularity at the mantle wedge corner is severely restricted by the grid refinement procedure.

singularity are not fully nullified, its influence is severely restricted by the grid refinement procedure. The point is reinforced by examining the mean global error, E_G, calculated as

$$E_G = \int_\Omega E_L d\Omega \,/\, \int_\Omega d\Omega \tag{20}$$

Results are presented in Table 3, demonstrating quantitatively that the refinement process undoubtedly has a positive influence on the global error. As the grids are adapted a dramatic decrease in error is observed. This is particularly true for the first remeshing, where E_G decreases by a factor of 4.5.

In summary, the adaptive strategies employed have significantly improved the accuracy of our SZ simulations. The refinement process has severely restricted the influence of the intersec-

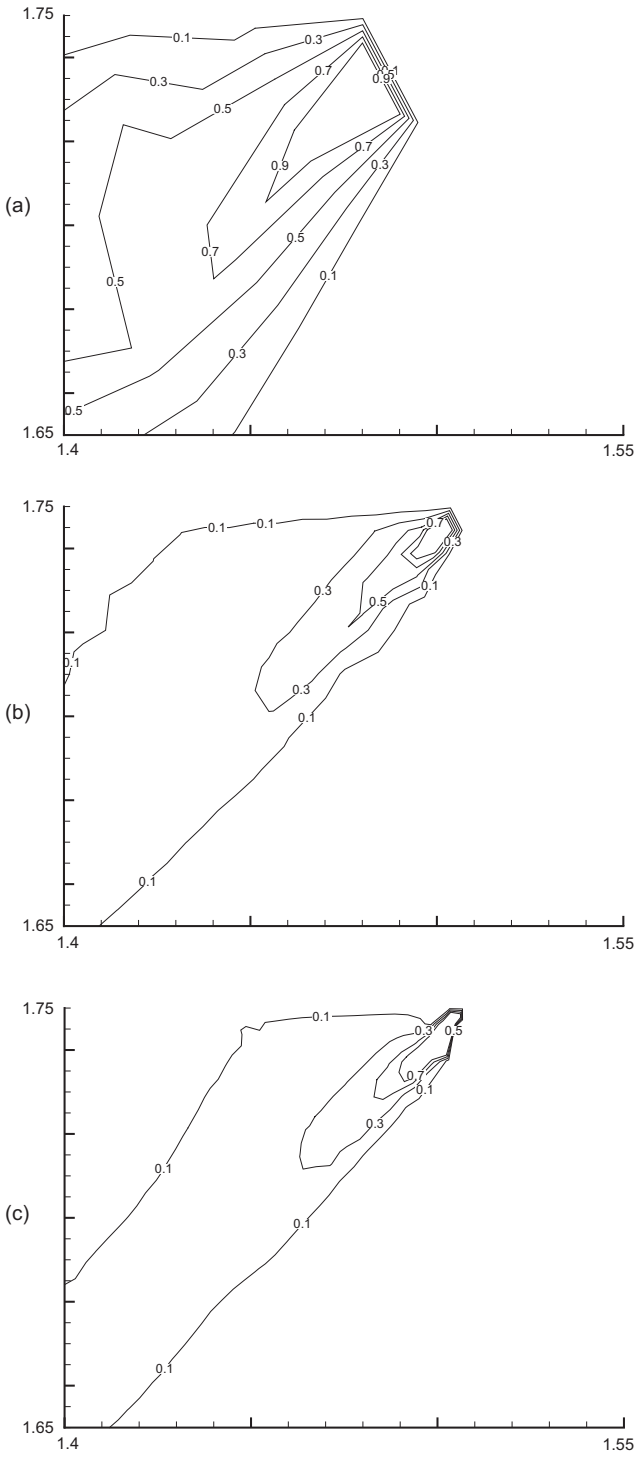

Figure 10: High resolution contour plots of the solution error, E_L, in the mantle wedge corner. Contour values range between 0.1 and 0.9, at a contour spacing on 0.2. (a) represents the solution error obtained on the initial grid, (b) the error after 1 remeshing, while (c) represents the final error, i.e. after 2 remeshings.

Stage	E_G
1	0.0117
2	0.0026
3	0.0022

Table 3: The mean global error, E_G, obtained at each stage during the subduction zone simulations.

tion singularities and, consequently, solution accuracy throughout the domain is improved. Our results suggest that an extension of this work to models with more realistic mantle rheologies, i.e. material properties, together with more Earth like surface plate behavior, incorporating solidification and localization phenomena, would be a worthwhile exercise. A true understanding of this system will only be gained by studying coupled crustal/mantle models. Such models naturally require fine resolution within the crust, where the plates fracture, bend and buckle, and coarser resolution as one descends into the mantle, where deformation occurs on a much larger scale. Error–guided grid adaptivity should therefore be an invaluable tool in simulating such dynamic systems.

4 Conclusions

An adaptive finite element procedure, investigated and validated previously by Davies *et al.* (2007), has been applied to simulations of two separate geodynamical processes—fluid flow at a mid–ocean ridge (MOR) and at a subduction zone (SZ). The method has refined the locations of thermal boundary layers wherever they are strong, i.e. at the ridge itself and along Earth's surface (MOR), and in the mantle wedge, along the margins of the descending plate and at Earth's surface (SZ). In such cases, the adapted grids maintain good solution accuracy and, through a series of remeshings, display the ability to gradually improve solution quality without necessarily increasing the total number of unknowns at each stage.

This investigation suggests that coupling adaptive strategies to more complex models will lead to a new class of geodynamical simulations, yielding greater insights into the complex processes at work within Earth's interior. It is therefore important that the geodynamical community begins to adopt such numerical schemes.

5 Acknowledgments

This project was enabled with the assistance of IBM Deep Computing at Swansea University, together with the Helix facility at Cardiff University. DRD would like to acknowledge support from both NERC and EPSRC as part of the Environmental Mathematics and Statistics (EMS) studentship programme (NER/S/E/2004/12725). The authors also thank Scott King

for help and support with ConMan and a number of colleagues, particularly Ben Evans, Richard Davies and Martin Wolstencroft, for helpful discussions.

References

Albers, M. and Christensen, U. R. Channeling of plume flow beneath mid-ocean ridges, *Earth Planet. Sci. Lett.*, 187, 207-220, 2001.

Andrews, D. J. and Sleep, N. Numerical modelling of tectonic flow behind island arcs, *Geophys. J. Roy. Astr. Soc.*, 38, 237-251, 1974.

Babuska, I. and Rheinbolt, W. C. *A posteriori* error estimates for the finite element method. *Int. J. Num. Meth.*, 12, 1597-1615, 1978.

Buck, W. R., Lavier, L. L. and Poliakov, A. N. B. Modes of faulting at mid-ocean ridges, *Nature*, 434, 719-723, 2005.

Carlsaw, H. S. and Jaeger, J. C. Conduction of heat in solids, 2nd edn. New York: Oxford University Press, 1959.

Christensen, U. R. Geodynamic models of deep subduction, *Phys. Earth Planet. Int.*, 127, 25-34, 2001.

Davies, G. F. and Richards, M. A. Mantle convection. *J. Geol.* 100, 151-206, 1992.

Davies, J. H. and Stevenson, D. J. Physical model of source region of subduction zone volcanics, *J. Geophys. Res.*, 97, 2037-2070, 1992.

Davies, D. R., Davies, J. H., Hassan, O., Morgan, K. and Nithiarasu, P. Investigations into the applicability of adaptive finite element methods to infinite Prandtl number thermal and thermochemical convection. *Geochem. Geophys. Geosys.*, 8, Q05010, doi:10.1029/2006GC001470, 2007.

George, A. J. Computer implementation of the finite element method, PhD thesis, STAN-CS-71-208, Stanford Univ., Stanford, Calif, 1971.

Hassan, O., Probert, E. J., Morgan, K. and Peraire, J. Mesh generation and adaptivity for the solution of compressible viscous high speed flows. *Int. J. Num. Meth. Eng.*, 38, 1123-1148, 1995.

Hughes, T. J. R. and Brooks, A. A multi-dimensional upwind scheme with no crosswind diffusion. in: *Finite element methods for convection dominated flows*, Vol. 34, 19-35, ASME, New York, 1979.

Iwamori, H. Transportation of H_2O and melting in subduction zones, *Earth Planet. Sci. Lett.*, 160, 65-80, 1998.

Kincaid, C. and Sacks, I. S. Thermal and dynamical evolution of the upper mantle in subduction zones, *J. Geophys. Res.*, 102, 12295-12315, 1997.

King, S. D., A. Raefsky, and B. H. Hager. ConMan: vectorizing a finite element code for incompressible two-dimensional convection in the Earth's mantle, *Phys. Earth Planet. Int., 59*, 195-207, 1990.

Kuhn, D. and Dahm, T. Simulation of magma ascent by dykes in the mantle beneath mid-ocean ridges, *J. Geodynamics*, 38, 147-159, 2004.

Lo, S. H. A new mesh generation scheme for arbitrary planar domains, *Int. J. Numer. Methods Eng.*, 21, 1403-1426, 1985.

Lohner, R., Morgan, K. and Zienkiewicz, O. C. An adaptive finite-element method for high-speed compressible flow, *Lect. Notes Phys.*, 218, 388-392, 1985.

Lohner, R. Mesh adaptation in fluid mechanics, *Eng. Fract. Mech.*, 50, 819-847, 1995.

Mayne, D. A., Usmani, A. S. and Crapper, M. h-adaptive finite element solution of high Rayleigh number thermally driven cavity problem, *Int. J. Num. Meth. Heat Fluid Flow*, 10, 598-615, 2000.

McKenzie, D. P. Speculations on the consequences and causes of plate motions, *Geophys. J. R. Astr. Soc.*, 18, 1-32, 1969.

Nielson, G. M., The side-vertex method for interpolation in triangles, *J. Approx. Theory, 25*, 318-336, 1979.

Nithiarasu, P. and Zienkiewicz, O. C. Adaptive mesh generation for fluid mechanics problems. *Int. J. Num. Meth. Eng.*, 47, 629-662, 2000.

Peacock, S. M. Thermal and petrologic structure of subduction zones. in: *Subduction Top to Bottom*, 119-113, Eds. Bebout, G. E., Scholl, D. W., Kirby, S. H. and Platt, J. P. *AGU Monograph*, 96, 1996.

Pelletier, D. and Ilinca, F. Adaptive finite element method for mixed convection. *J. Thermo. Heat. Trans.*, 9, 708-714, 1995.

Peraire, J., M. Vahdati, K. Morgan, K. and O. C. Zienkiewicz, Adaptive remeshing for compressible flow computations, *J. Comp. Phys.,* 72, 449-466, 1987.

Turcotte, D. L. and Schubert, G. Application of continuum physics to geological problems, Wiley, New York, 1982.

Turcotte, D. L. and Schubert, G. Geodynamics. 2nd ed., Cambridge University Press, 2002.